Are narrow-line Seyfert 1 galaxies highly accreting low-M_{BH} AGNs?

James K. Williams,[1]⋆ Mario Gliozzi[1] and Ross V. Rudzinsky[2]

[1]*Department of Physics and Astronomy, George Mason University, 4400 University Drive, Fairfax, VA 22030, USA*
[2]*Department of Physics, University of California, 366 LeConte Hall, Berkeley, CA 94720, USA*

ABSTRACT

In this work, we test the hypothesis that narrow-line Seyfert 1 galaxies (NSL1s) are active galactic nuclei in their early phase and are therefore younger and more active than the more common broad-line Seyfert 1 galaxies (BLS1s). If that is true, then NLS1s should, on average, have lower black hole (BH) masses and higher accretion rates than BLS1s. To test this, we use a sample of 35 NLS1s and 54 BLS1s with similar X-ray luminosity distributions and good *XMM–Newton* observations. To determine the BH mass M_{BH}, we apply an X-ray scaling method that is independent of any assumptions on the broad-line region dynamics and the inclination of the objects. We find that, on average, NLS1s have lower BH masses, but the difference between the average M_{BH} of NLS1s and BLS1s in our sample is only marginally significant (at the 2.6σ level). According to a Kolmogorov–Smirnov test, the distribution of M_{BH} values of NLS1s is different from that of BLS1s at the 99 per cent confidence level. Even stronger differences between NLS1s and BLS1s are inferred when the accretion rate distributions of NLS1s are compared to BLS1s, suggesting that the two populations are indeed distinct. Our study also indicates that the M_{BH} values (both for NLS1s and BLS1s) determined with the X-ray scaling method are fully consistent with those obtained using reverberation mapping.

Key words: galaxies: active – galaxies: nuclei – X-rays: galaxies.

1 INTRODUCTION

Narrow-line Seyfert 1 galaxies (NLS1s) are distinguished from the more common broad-line Seyfert 1 galaxies (BLS1s) by the properties of their emission lines. In the optical spectrum, NLS1s have an [O III]/H β ratio of less than 3 and a full width at half-maximum H β of less than 2000 km s^{-1}. In the X-ray spectrum, NLS1s tend to have steep spectra and strong variability. These differences have led to the hypothesis that NLS1s are active galactic nuclei (AGNs) in their early phase and therefore are younger and more active (e.g. Boroson & Green 1992; Grupe & Mathur 2004). If NLS1s are younger and more active, they should, on average, have lower black hole (BH) masses and higher accretion rates than BLS1s.

Several optical estimates of the BH mass M_{BH} of NLS1s suggested that NLS1s lie below the M_{BH}–σ_{bulge} curve (σ_{bulge} is the velocity dispersion of the galaxy's bulge), which implies that they are accreting at higher rates than BLS1s (e.g. Grupe & Mathur 2004; Mathur & Grupe 2005a,b). However, other research challenged the use of optical methods for determining M_{BH} in NLS1s on the basis that highly accreting objects produce high radiation pressure that partially counteracts the action of the BH gravitational pull,

leading to values of M_{BH} that are systematically underestimated (e.g. Marconi et al. 2008). Another possibility is that NLS1s are simply ordinary Seyfert 1s with a disc-shaped broad-line region (BLR) and a line of sight that is pole-on; in that case, the difference between NLS1s and BLS1s disappears (e.g. Decarli et al. 2008). Furthermore, past studies suggest that NLS1s may not be a homogeneous class. For example, optically selected and X-ray-selected NLS1s appear to have different properties (e.g. Grupe 2004). In addition, recent results from *Fermi LAT* suggest that a small subset of NLS1s is likely to be jet-dominated (e.g. Foschini et al. 2015).

To test the hypothesis introduced above, it is crucial to make accurate measurements of M_{BH} and accretion rate $\dot{m}$. The best and most direct way of obtaining M_{BH} is by dynamical methods. For our own Galaxy, we can derive M_{BH} by directly observing the motion of gas and stars near the BH, but this requires that the region of influence of the BH can be resolved by our telescope. Therefore, this method works only for galaxies that are nearby and that have weakly active nuclei. For AGNs farther away, the best method we have is reverberation mapping (RM), which derives M_{BH} by measuring the size and kinematics of the BLR by observing the light-speed time delay τ as changes in the continuum emission propagate out from the central accretion disc and cause changes in lines emitted by
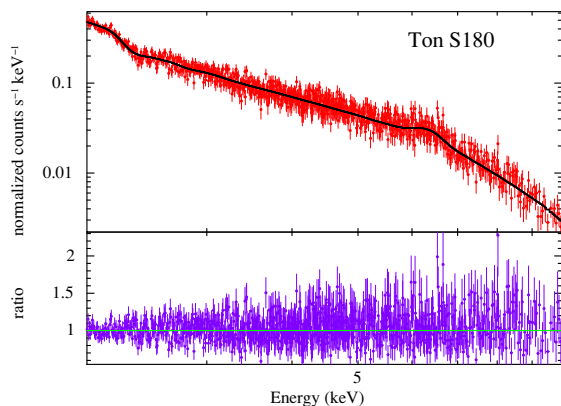
⋆ E-mail: jwilli91@masonlive.gmu.edu

Figure 1. Best fit for the model wabs∗(bmc+zgauss) for Ton S180. The lower panel shows the residuals.

structures farther away from the central BH (e.g. Peterson & Horne 2006).

However, these direct methods have some limitations when applied to our particular problem. Applying the most direct method for AGNs, RM, to highly accreting objects can be questionable when the dynamics of the BLR may be affected by radiation pressure and not just M_{BH} gravitational force, or with small viewing angles, or both. For NLS1s (and highly accreting objects in general), it is important to use methods to constrain M_{BH} that are independent of any assumptions on the BLR dynamics and geometry. Therefore, for this work we used an X-ray scaling method of determining M_{BH} (Shaposhnikov & Titarchuk 2009). The X-ray scaling method does not depend on any assumptions about the BLR, nor does it need to make a correction for radiation pressure.

It is now generally accepted that hard X-rays (>2 keV) are produced primarily by inverse Comptonization, where seed photons, originally emitted in the optical and UV directly from the accretion disc, are upscattered several times and become hard X-rays in the corona. The energy band of the original photons depends heavily on M_{BH} and $\dot{m}$. This process appears to be ubiquitous in all BH systems, which is a major motivation for using X-rays to measure M_{BH}. It means we can use the X-ray scaling method for all types of BHs. Indeed, this scaling method, originally developed for Galactic black holes (GBHs; Shaposhnikov & Titarchuk 2009) was later successfully extended to supermassive BHs (Gliozzi et al. 2011) and also to ultraluminous X-ray sources, which may host intermediate-mass BHs (Jang et al. 2018). In the X-ray scaling method, the value of M_{BH} for any BH system, accreting at a moderate or a high level, can be obtained by scaling the M_{BH} of a reference source, which is a stellar-mass BH in a binary system whose parameters are tightly constrained via direct methods. The scaling factor is determined by the ratio of the normalization parameter in the Comptonization model used to fit the X-ray spectrum of the target to the analogous parameter of the reference source. Further details of this method are provided in Section 4. In principle, the method can be used for any BH for which most of the X-rays are produced by Comptonization, although care must be taken to account for absorption and reflection.

In this work, we applied the X-ray scaling method to a subsample of NLS1s and BLS1s drawn from the flux-limited sample compiled by Zhou & Zhang (2010) using *XMM–Newton* observations. Our goal was to investigate whether the distribution of M_{BH} and $\dot{m}$ of NLS1s is statistically different from that of BLS1s. In Section 2, we briefly describe the sample and the data reduction. Section 3 reports the results of our X-ray spectral analysis. In Section 4, we

show how we derived the BH masses and accretion rates using the X-ray scaling method and compare their respective distributions for NLS1s and BLS1s. Finally, in Section 5, we summarize our main findings and discuss their implications.

Throughout the paper, we use a cosmology based on a ΛCDM model with $H_0 = 71 \, \text{km s}^{-1} \, \text{Mpc}^{-1}$, $\Omega_m = 0.27$, and $\Omega_v = 0.73$.

2 DATA REDUCTION

We took our NLS1 and BLS1 samples from the flux-limited sample ($f_{2-10\,\text{keV}} \geq 1 \times 10^{-12} \, \text{erg s}^{-1}\text{cm}^{-2}$) of Zhou & Zhang (2010), which contains 114 radio-quiet type I AGNs with hard X-ray (2–10 keV) luminosities from 10^{41} to 10^{45} erg s^{-1}. Of the 114 AGNs in their sample, 16 are narrow emission line galaxies (NELGs), and those were not processed or used in this study. That left a total of 98, which we divided into a sample of 36 NLS1s and a second sample of 62 BLS1s. The two samples, which are constructed based on the similarity of their X-ray luminosity distributions, contain the brightest members of BLS1s and NLS1s observed by *XMM–Newton*, and hence may represent the brightest tails of the two populations rather than the whole populations. Therefore, we acknowledge that our samples are starting points and not perfectly random. All 98 AGNs were processed with the *XMM–Newton* Science Analysis System (SAS) version 15.0.0, and for each source, ancillary response (ARF) and redistribution matrix (RMF) files were created. For sources with more than one *XMM–Newton* observation, we chose the most recent one with a duration of at least 10 ks, using the EPIC cameras (e.g. Strüder et al. 2001; Turner et al. 2001). Source photons were extracted in a circle with a radius of 30 arcsec centred on the source from the EPIC pn image, and the background was selected from a source-free region on the same CCD as the source and with a radius of 60 arcsec. Spectra were rebinned with GRPPHA to have at least 20 counts per bin, although for some faint sources we used 15 instead. The recorded events were screened to remove known hot pixels and data affected by background flares, as recommended by the SAS user guide.

To assess the presence of pile-up, for each source we verified the EPIC camera observing mode and compared the background-subtracted source count rate with the appropriate threshold count rates above which sources are expected to suffer from pile-up according to the *XMM–Newton Users Handbook*. Of the 89 AGNs for which we computed M_{BH}, 84 have count rates well below the pile-up thresholds. For the remaining five sources, following the SAS user guide, we quantified the incidence of pile-up using the SAS task EPATPLOT. This tool provides plots of the distributions of single and double patterns, which are very sensitive to pile-up effects: deviations from the model curves indicate the presence of pile-up. Of the five bright AGNs, only Mrk 1383 and Mrk 841 show clear deviations from the theoretical single and double patterns curves, indicating that these two sources are indeed affected by pile-up (the level of pile-up was estimated using WEBPIMMS and it is of the order of 7 per cent for Mrk 1383 and 10 per cent for Mrk 841). Following the procedure recommended by the SAS user guide to mitigate the effects of pile-up on EPIC camera data, we excised the inner part of the extraction region using an annulus with inner and outer radii of 10 and 40 arcsec, respectively. After checking with EPATPLOT that the new extraction regions yielded the correct single and double patterns, we extracted the spectra and ran the ARFGEN task again to account for the flux loss. A comparison of the spectra of Mrk 1383 and Mrk 841 using annular extraction regions with those using circular regions shows that the latter are fitted by flatter photon indices, as expected for piled-up spectra.

Table 1. NLS1 spectral data.

Name (1)	Model (2)	kT (3)	α (4)	log A (5)	Norm (6)
Mrk 335	wabs*(bmc+zgauss)	$0.28^{+0.02}_{-0.02}$	$0.90^{+0.05}_{-0.05}$	-0.44	$1.9^{+0.1}_{-0.1} \times 10^{-4}$
I Zw 1	wabs*(bmc+zgauss)	$0.20^{+0.04}_{-0.20}$	$1.25^{+0.05}_{-0.06}$	0.17	$1.6^{+2.2}_{-0.2} \times 10^{-4}$
Ton S180	wabs*(bmc+zgauss)	$0.34^{+0.04}_{-0.05}$	$1.05^{+0.07}_{-0.04}$	0.29	$5.3^{+0.4}_{-0.2} \times 10^{-5}$
Mrk 359	wabs*(bmc+zgauss)	$0.26^{+0.03}_{-0.03}$	$0.63^{+0.08}_{-0.08}$	0.15	$8.6^{+0.2}_{-0.2} \times 10^{-5}$
Mrk 1014	wabs*bmc	0.30	$1.02^{+0.21}_{-0.19}$	0.34	$1.1^{+0.1}_{-0.9} \times 10^{-5}$
Mrk 586	wabs*bmc	0.19	$1.21^{+0.08}_{-0.08}$	1.22	$2.0^{+0.2}_{-0.2} \times 10^{-5}$
Mrk 1044	wabs*bmc	$0.34^{+0.03}_{-0.03}$	$0.93^{+0.05}_{-0.04}$	0.24	$1.4^{+0.1}_{-0.1} \times 10^{-4}$
RBS 416	wabs*bmc	$0.26^{+0.11}_{-0.27}$	$0.95^{+0.08}_{-0.08}$	0.73	$1.4^{+0.2}_{-0.3} \times 10^{-5}$
HE 0450$-$2958	wabs*(bmc+zgauss)	$0.42^{+0.10}_{-0.42}$	$1.01^{+0.15}_{-0.11}$	0.75	$2.2^{+0.1}_{-0.4} \times 10^{-5}$
PKS 0558$-$504	wabs*bmc	$0.34^{+0.03}_{-0.03}$	$0.96^{+0.03}_{-0.03}$	0.34	$1.9^{+0.1}_{-0.1} \times 10^{-4}$
Mrk 110	wabs*(bmc+zgauss)	$0.30^{+0.02}_{-0.02}$	$0.64^{+0.03}_{-0.03}$	0.50	$3.0^{+0.1}_{-0.1} \times 10^{-4}$
PG 0953+414	wab*bmc	$0.33^{+0.10}_{-0.34}$	$0.91^{+0.11}_{-0.08}$	0.68	$3.1^{+0.1}_{-0.1} \times 10^{-5}$
RE J1034+396	wabs*(bmc+zgauss)	$0.31^{+0.16}_{-0.11}$	$0.90^{+0.30}_{-0.50}$	0.04	$1.3^{+0.5}_{-0.2} \times 10^{-5}$
PG 1115+407	wabs*bmc	$0.39^{+0.09}_{-0.39}$	$0.96^{+0.09}_{-0.13}$	0.32	$1.5^{+2.5}_{-0.1} \times 10^{-5}$
PG 1116+215	wabs*(bmc+zgauss)	$0.31^{+0.06}_{-0.08}$	$0.82^{+0.04}_{-0.04}$	0.85	$2.9^{+0.1}_{-0.1} \times 10^{-5}$
NGC 4051	wabs*(bmc+zgauss)	$0.44^{+0.06}_{-0.07}$	$0.54^{+0.05}_{-0.05}$	2.00	$1.0^{+0.1}_{-0.1} \times 10^{-4}$
PG 1211+143	wabs*(bmc+zgauss)	$0.15^{+0.08}_{-0.15}$	$1.02^{+0.02}_{-0.02}$	2.00	$3.1^{+0.4}_{-0.1} \times 10^{-5}$
Mrk 766	wabs*(bmc+zgauss)	$0.25^{+0.05}_{-0.26}$	$1.02^{+0.03}_{-0.03}$	2.00	$1.5^{+0.1}_{-0.1} \times 10^{-4}$
Was 61	wabs*bmc	$0.31^{+0.02}_{-0.02}$	$1.16^{+0.06}_{-0.06}$	-0.13	$1.3^{+0.1}_{-0.1} \times 10^{-4}$
PG 1244+026	wabs*bmc	$0.29^{+0.02}_{-0.02}$	$1.33^{+0.09}_{-0.09}$	-0.30	$7.6^{+0.9}_{-0.8} \times 10^{-5}$
PG 1322+659	wabs*bmc	$0.30^{+0.11}_{-0.08}$	$1.12^{+0.30}_{-0.37}$	-0.14	$3.1^{+1.4}_{-0.7} \times 10^{-5}$
MCG$-6-30-15$	wabs*(bmc+zgauss)	$0.25^{+0.01}_{-0.01}$	$0.88^{+0.03}_{-0.03}$	-0.32	$7.6^{+0.2}_{-0.2} \times 10^{-4}$
IRAS 13349+2438	wabs*(bmc+zgauss)	$0.61^{+0.04}_{-0.04}$	$1.28^{+0.13}_{-0.11}$	2.00	$3.4^{+0.1}_{-0.1} \times 10^{-5}$
PG 1402+261	wabs*bmc	$0.38^{+0.11}_{-0.15}$	$0.75^{+0.22}_{-0.16}$	0.31	$1.9^{+0.2}_{-0.2} \times 10^{-5}$
NGC 5506	wabs*(bmc+2zgauss)	$0.38^{+0.02}_{-0.02}$	$0.76^{+0.01}_{-0.01}$	2.00	$1.1^{+0.1}_{-0.1} \times 10^{-3}$
PG 1440+356	wabs*bmc	$0.30^{+0.09}_{-0.10}$	$0.96^{+0.14}_{-0.13}$	0.30	$2.4^{+0.3}_{-0.2} \times 10^{-5}$
PG 1448+273	wabs*bmc	$0.28^{+0.04}_{-0.03}$	$1.30^{+0.17}_{-0.19}$	-0.45	$9.8^{+2.5}_{-1.9} \times 10^{-5}$
Mrk 493	wabs*bmc	$0.29^{+0.05}_{-0.07}$	$0.95^{+0.05}_{-0.05}$	0.75	$1.9^{+0.1}_{-0.1} \times 10^{-5}$
IRAS 17020+4544	wabs*(bmc+zgauss)	$0.26^{+0.04}_{-0.03}$	$1.15^{+0.04}_{-0.05}$	0.34	$9.4^{+0.6}_{-0.6} \times 10^{-5}$
PDS 456	wabs*(bmc+zgauss)	$0.10^{+0.28}_{-0.10}$	$1.06^{+0.02}_{-0.02}$	1.12	$3.1^{+0.7}_{-0.2} \times 10^{-5}$
Mrk 896	wabs*bmc	$0.28^{+0.11}_{-0.28}$	$1.00^{+0.08}_{-0.08}$	0.96	$3.8^{+1.4}_{-0.8} \times 10^{-5}$
Mrk 1513	wabs*(bmc+zgauss)	$0.08^{+0.16}_{-0.08}$	$0.69^{+0.04}_{-0.04}$	0.35	$2.6^{+0.9}_{-1.0} \times 10^{-5}$
II Zw 177	wabs*bmc	$0.21^{+0.16}_{-0.21}$	$1.40^{+0.16}_{-0.15}$	1.07	$1.5^{+7.2}_{-0.3} \times 10^{-5}$
Ark 564	wabs*bmc	$0.30^{+0.02}_{-0.03}$	$1.44^{+0.03}_{-0.02}$	0.27	$4.1^{-0.3}_{-0.2} \times 10^{-4}$
AM 2354$-$304	wabs*bmc	$0.52^{+0.18}_{-0.51}$	$1.15^{+0.60}_{-0.36}$	0.80	$4.2^{+2.6}_{-1.4} \times 10^{-5}$

Note: Columns: 1 = AGN name. 2 = XSPEC model used. 3 = Temperature of thermal seed photons in keV. 4 = Energy spectral index ($\alpha = \Gamma - 1$). 5 = Logarithm of the A parameter (which is related to the Comptonization fraction f by $f = A/(1 + A)$). 6 = BMC normalization. Numbers in columns 3–6 without error ranges were frozen at their best-fitting values.

3 X-RAY SPECTRAL ANALYSIS

All the AGNs were fitted using XSPEC (Arnaud 1996). Since the X-ray scaling method depends only on the Comptonization component, we restricted the spectral fitting range to 2–10 keV. This also reduces possible spectral-fitting complications related to the characterization of the soft X-ray component. Our basic XSPEC model was wabs*bmc. WABS models both Galactic and intrinsic absorption. BMC is the bulk motion Comptonization model (Titarchuk, Mastichiadis & Kylafis 1997). When needed, Gaussian lines were added, most commonly to model prominent Fe K α emission lines near 6.4 keV.

BMC has the advantage of being generic enough to describe both thermal Comptonization and bulk motion Comptonization equally well. The model convolves the seed photons and a generic Comptonization Green's function giving a power law, which usually produces a good fit.

The BMC model has the following four parameters: (1) kT, the temperature of the thermal seed photons, (2) α, the energy spectral index, (3) log A, the logarithm of the A parameter, and (4) N_{BMC}, the BMC normalization. The spectral index α is related to the photon index Γ by $\Gamma = 1 + \alpha$. The A parameter is related to the Comptonization fraction f by $f = A/(1 + A)$. N_{BMC} is a function of luminosity L and distance d and is proportional to L/d^2. In our analysis, we

Table 2. BLS1 spectral data.

Name	Model	kT	α	$\log A$	Norm
(1)	(2)	(3)	(4)	(5)	(6)
PG 0052+251	wabs*bmc	$0.28^{+0.11}_{-0.16}$	$0.83^{+0.15}_{-0.06}$	0.53	$5.7^{+0.8}_{-2.5} \times 10^{-5}$
Q 0056$-$363	wabs*bmc	$0.35^{+0.08}_{-0.09}$	$0.78^{+0.11}_{-0.09}$	0.36	$3.1^{+0.1}_{-0.1} \times 10^{-5}$
Mrk 1152	wabs*(bmc+zgauss)	$0.33^{+0.10}_{-0.09}$	$0.49^{+0.08}_{-0.10}$	0.61	$4.4^{+0.8}_{-0.6} \times 10^{-5}$
ESO 244$-$G17	wabs*bmc	$0.24^{+0.06}_{-0.24}$	$0.68^{+0.09}_{-0.10}$	0.40	$3.3^{+0.1}_{-1.9} \times 10^{-5}$
Fairall 9	wabs*(bmc+zgauss)	$0.48^{+0.10}_{-0.48}$	$0.81^{+0.17}_{-0.14}$	0.59	$2.4^{+0.1}_{-1.0} \times 10^{-4}$
Mrk 590	wabs*(bmc+zgauss)	$0.24^{+0.04}_{-0.06}$	$0.57^{+0.06}_{-0.06}$	0.36	$6.4^{+0.3}_{-0.5} \times 10^{-5}$
ESO 198$-$G24	wabs*(bmc+zgauss)	$0.31^{+0.03}_{-0.03}$	$0.59^{+0.03}_{-0.03}$	0.52	$1.0^{+0.1}_{-0.1} \times 10^{-4}$
Fairall 1116	wabs*(bmc+zgauss)	$0.26^{+0.09}_{-0.11}$	$0.81^{+0.06}_{-0.07}$	0.58	$5.3^{+0.2}_{-0.3} \times 10^{-5}$
1H 0419$-$577	wabs*bmc	$0.30^{+0.02}_{-0.02}$	$0.59^{+0.03}_{-0.04}$	0.40	$1.4^{+0.1}_{-0.1} \times 10^{-4}$
3C 120	wabs*(bmc+2zgauss)	$0.33^{+0.03}_{-0.02}$	$0.67^{+0.03}_{-0.03}$	0.46	$4.9^{+0.1}_{-0.1} \times 10^{-4}$
H 0439$-$272	wabs*bmc	$0.40^{+0.07}_{-0.13}$	$0.70^{+0.10}_{-0.06}$	0.52	$6.1^{+0.8}_{-0.6} \times 10^{-5}$
MCG$-$01$-$13$-$25	wabs*bmc	$0.29^{+0.09}_{-0.09}$	$0.55^{+0.11}_{-0.16}$	0.39	$1.3^{+0.2}_{-0.1} \times 10^{-4}$
Ark 120	wabs*(bmc+2zgauss)	$0.28^{+0.01}_{-0.01}$	$0.78^{+0.02}_{-0.02}$	0.20	$4.6^{+0.1}_{-0.1} \times 10^{-4}$
MCG$-$02$-$14$-$09	wabs*(bmc+zgauss)	$0.36^{+0.03}_{-0.04}$	$0.73^{+0.04}_{-0.03}$	0.54	$4.4^{+0.1}_{-0.1} \times 10^{-5}$
MCG+8$-$11$-$11	wabs*(bmc+zgauss)	$0.36^{+0.05}_{-0.05}$	$0.54^{+0.04}_{-0.03}$	0.66	$4.4^{+0.3}_{-0.3} \times 10^{-4}$
H 0557$-$385	wabs*bmc	$0.09^{+0.37}_{-0.09}$	$0.71^{+0.06}_{-0.06}$	0.43	$3.4^{+2.0}_{-1.1} \times 10^{-4}$
PMN J0623$-$6436	wabs*bmc	$0.43^{+0.12}_{-0.43}$	$0.62^{+0.25}_{-0.16}$	0.50	$3.9^{+0.6}_{-2.2} \times 10^{-5}$
ESO 209$-$G12	wabs*(bmc+zgauss)	$0.22^{+0.10}_{-0.22}$	$0.73^{+0.07}_{-0.10}$	0.47	$7.9^{+0.5}_{-4.2} \times 10^{-5}$
PG 0804+761	wabs*(bmc+zgauss)	$0.28^{+0.06}_{-0.14}$	$1.01^{+0.04}_{-0.04}$	0.82	$9.6^{+0.4}_{-0.2} \times 10^{-5}$
Fairall 1146	wabs*(bmc+zgauss)	$0.25^{+0.08}_{-0.24}$	$0.80^{+0.08}_{-0.09}$	0.55	$1.3^{+0.1}_{-0.8} \times 10^{-4}$
PG 0844+349	wabs*(bmc+zgauss)	$0.22^{+0.42}_{-0.22}$	$0.23^{+0.35}_{-0.23}$	0.44	$9.1^{+17.0}_{-7.1} \times 10^{-6}$
MCG+04$-$22$-$42	wabs*(bmc+zgauss)	$0.41^{+0.06}_{-0.08}$	$0.67^{+0.07}_{-0.06}$	0.51	$1.7^{+0.1}_{-0.1} \times 10^{-4}$
PG 0947+396	wabs*(bmc+zgauss)	$0.31^{+0.14}_{-0.13}$	$0.64^{+0.14}_{-0.19}$	0.44	$1.8^{+0.3}_{-0.1} \times 10^{-5}$
HE 1029$-$1401	wabs*(bmc+zgauss)	$0.28^{+0.02}_{-0.02}$	$0.83^{+0.03}_{-0.04}$	0.96	$1.7^{+0.1}_{-0.1} \times 10^{-4}$
PG 1048+342	wabs*(bmc+zgauss)	$0.32^{+0.13}_{-0.32}$	$0.70^{+0.10}_{-0.09}$	0.76	$1.3^{+0.1}_{-1.3} \times 10^{-5}$
NGC 3516	wabs*(bmc+zgauss)	$0.47^{+0.02}_{-0.02}$	$0.73^{+0.02}_{-0.02}$	2.00	$4.1^{+0.1}_{-0.1} \times 10^{-4}$
PG 1114+445	wabs*bmc	$0.11^{+0.12}_{-0.11}$	$0.38^{+0.08}_{-0.08}$	0.49	$1.2^{+0.8}_{-1.2} \times 10^{-5}$
NGC 3783	wabs*(bmc+zgauss)	$0.37^{+0.02}_{-0.02}$	$0.50^{+0.01}_{-0.01}$	2.00	$4.8^{+0.1}_{-0.2} \times 10^{-4}$
HE 1143$-$1810	wabs*(bmc+zgauss)	$0.34^{+0.03}_{-0.03}$	$0.65^{+0.04}_{-0.04}$	0.36	$3.2^{+0.1}_{-0.1} \times 10^{-4}$
PG 1202+281	wabs*bmc	$0.38^{+0.11}_{-0.13}$	$0.59^{+0.15}_{-0.15}$	0.45	$3.9^{+0.5}_{-0.3} \times 10^{-5}$
Mrk 205	wabs*(bmc+zgauss)	$0.14^{+0.07}_{-0.15}$	$1.00^{+0.02}_{-0.02}$	2.00	$1.1^{+0.1}_{-0.1} \times 10^{-4}$
Ark 374	wabs*bmc	$0.36^{+0.07}_{-0.07}$	$0.79^{+0.16}_{-0.16}$	0.09	$4.9^{+0.4}_{-0.2} \times 10^{-5}$
NGC 4593	wabs*(bmc+zgauss)	$0.38^{+0.04}_{-0.05}$	$0.57^{+0.05}_{-0.05}$	0.48	$2.7^{+0.1}_{-0.1} \times 10^{-4}$
PG 1307+085	wabs*(bmc+zgauss)	$0.39^{+0.19}_{-0.39}$	$0.59^{+0.22}_{-0.13}$	2.00	$1.5^{+0.3}_{-1.5} \times 10^{-5}$
4U 1344$-$60	wabs*bmc	$0.36^{+0.12}_{-0.36}$	$0.51^{+0.07}_{-0.06}$	0.85	$5.4^{+0.9}_{-5.4} \times 10^{-5}$
IC 4329A	wabs*(bmc+2zgauss)	$0.36^{+0.02}_{-0.02}$	$0.63^{+0.01}_{-0.01}$	0.59	$9.9^{+0.1}_{-0.1} \times 10^{-4}$
Mrk 279	wabs*(bmc+zgauss)	$0.38^{+0.05}_{-0.06}$	$0.64^{+0.06}_{-0.05}$	0.47	$2.6^{+0.1}_{-0.1} \times 10^{-4}$
PG 1352+183	wabs*bmc	$0.26^{+0.02}_{-0.02}$	$1.14^{+0.26}_{-0.27}$	-1.17	$3.7^{+1.4}_{-0.9} \times 10^{-4}$
PG 1415+451	wabs*(bmc+zgauss)	$0.37^{+0.11}_{-0.18}$	$0.87^{+0.27}_{-0.18}$	0.23	$1.4^{+0.4}_{-0.1} \times 10^{-5}$
NGC 5548	wabs*(bmc+2zgauss)	$0.24^{+0.01}_{-0.01}$	$0.45^{+0.02}_{-0.02}$	0.23	$3.0^{+0.1}_{-0.1} \times 10^{-4}$
PG 1416$-$129	wabs*bmc	$0.36^{+0.03}_{-0.03}$	$0.54^{+0.13}_{-0.14}$	-0.02	$5.5^{+0.3}_{-0.3} \times 10^{-5}$
PG 1425+267	wabs*bmc	$0.47^{+0.13}_{-0.47}$	$0.57^{+0.16}_{-0.13}$	2.00	$1.5^{+0.2}_{-1.0} \times 10^{-5}$
Mrk 1383	wabs*(bmc+zgauss)	$0.50^{+0.10}_{-0.50}$	$0.79^{+0.19}_{-0.16}$	0.49	$9.6^{+0.6}_{-0.5} \times 10^{-5}$
PG 1427+480	wabs*bmc	$0.33^{+0.05}_{-0.05}$	$0.93^{+0.20}_{-0.22}$	-0.22	$2.8^{+0.5}_{-0.3} \times 10^{-5}$
Mrk 841	wabs*bmc	$0.25^{+0.05}_{-0.05}$	$0.75^{+0.07}_{-0.08}$	0.31	$1.8^{+0.1}_{-0.1} \times 10^{-4}$
Mrk 290	wabs*(bmc+zgauss)	$0.23^{+0.11}_{-0.25}$	$0.56^{+0.10}_{-0.10}$	0.47	$6.8^{+1.3}_{-4.7} \times 10^{-5}$
Mrk 876	wabs*bmc	$0.30^{+0.02}_{-0.03}$	$0.50^{+0.44}_{-0.33}$	-0.99	$3.7^{+1.0}_{-0.3} \times 10^{-4}$
PG 1626+554	wabs*bmc	$0.33^{+0.09}_{-0.13}$	$0.50^{+0.38}_{-0.35}$	0.14	$3.9^{+2.4}_{-0.3} \times 10^{-5}$
IGR J17418$-$1212	wabs*bmc	$0.40^{+0.11}_{-0.40}$	$0.77^{+0.12}_{-0.16}$	0.49	$1.5^{+0.1}_{-0.1} \times 10^{-4}$
Mrk 509	wabs*bmc	$0.36^{+0.02}_{-0.02}$	$0.61^{+0.02}_{-0.02}$	0.39	$5.7^{+0.1}_{-0.1} \times 10^{-4}$

Table 2 – *continued*

Name	Model	kT	α	$\log A$	Norm
(1)	(2)	(3)	(4)	(5)	(6)
Mrk 304	wabs*(bmc+zgauss)	$0.05^{+1.19}_{-0.05}$	$0.79^{+0.19}_{-0.18}$	1.26	$2.4^{+0.1}_{-1.0} \times 10^{-5}$
MR 2251−178	wabs*bmc	$0.33^{+0.06}_{-0.05}$	$0.53^{+0.03}_{-0.04}$	0.70	$4.2^{+0.3}_{-0.2} \times 10^{-4}$
NGC 7469	wabs*(bmc+zgauss)	$0.39^{+0.02}_{-0.02}$	$0.62^{+0.02}_{-0.02}$	0.47	$3.4^{+0.1}_{-0.1} \times 10^{-4}$
Mrk 926	wabs*bmc	$0.24^{+0.04}_{-0.05}$	$0.60^{+0.04}_{-0.05}$	0.38	$3.0^{+0.1}_{-0.2} \times 10^{-4}$

Note: Columns: 1 = AGN name. 2 = XSPEC model used. 3 = Temperature of thermal seed photons in keV. 4 = Energy spectral index ($\alpha = \Gamma - 1$). 5 = Logarithm of the A parameter (which is related to the Comptonization fraction f by $f = A/(1 + A)$). 6 = BMC normalization. Numbers in columns 3–6 without error ranges were frozen at their best-fitting values.

started with reasonable guesses for these parameters and let them vary.

To give just one illustration of the model, Fig. 1 shows a plot of the NLS1 Ton S180 spectrum fitted with the model wabs*(bmc+zgauss), which yielded the following best-fitting parameters: $kT = 0.34^{+0.04}_{-0.05}$, $\alpha = 1.05^{+0.07}_{-0.04}$, $\log A = 0.29$, and $N_{\rm BMC} = 5.3^{+0.4}_{-0.2} \times 10^{-5}$, with a reduced χ^2 of 1.00 for 889 degrees of freedom.

The results of our systematic and homogeneous spectral analysis of the NLS1 and BLS1 samples are reported in Tables 1 and 2, which show the best-fitting values for 89 AGNs. For the other nine AGNs, the X-ray spectrum appears to be dominated by reflection or absorption or both, which hampers the proper characterization of the primary X-ray component, which is a requirement for applying the scaling method (see the next section for further details). All AGNs were reasonably well fitted with our baseline model, the reduced χ^2 ranging from 0.63 to 1.37 with an average of 0.99. For NLS1s, α ranges from 0.54 to 1.44 with a mean of 1.00, whereas for BLS1s, α ranges from 0.23 to 1.14 with a mean of 0.67, confirming that NLS1s have on average steeper X-ray slopes. On the other hand, for the other three parameters, kT, $\log A$, and $N_{\rm BMC}$, there are no significant differences between NLS1s and BLS1s. For NLS1s, kT ranges from 0.08 to 0.61 with a mean of 0.30, whereas for BLS1s, kT ranges from 0.05 to 0.56 with a mean of 0.32. For NLS1s, $\log A$ ranges from −0.45 to 2.00 with a mean of 0.60, whereas for BLS1s, $\log A$ ranges from −1.17 to 2.00 with a mean of 0.55. For NLS1s, $N_{\rm BMC}$ ranges from 1.08×10^{-5} to 1.10×10^{-3} with a mean of 1.28×10^{-4}, whereas for BLS1s, $N_{\rm BMC}$ ranges from 9.1×10^{-6} to 9.93×10^{-4} with a mean of 1.81×10^{-4}.

Based on our spectral analysis, NLS1s have 2–10 keV luminosity values that range from 1.4×10^{41} to 7.6×10^{44} erg s^{-1} with a mean of 9.7×10^{43} erg s^{-1}. BLS1s, on the other hand, have $L_{\rm X}$ values that range from 2.1×10^{42} to 6.0×10^{44} erg s^{-1} with a mean of 1.1×10^{44} erg s^{-1}.

In summary, our homogeneous analysis of NLS1s and BLS1s indicates that the two samples have the same characteristics based on X-ray luminosity and spectral parameters, with the notable exception of the spectral index, which is significantly steeper in NLS1s.

4 BH MASS AND ACCRETION RATE ESTIMATES

We determined the BH mass of the AGNs in our sample by applying the X-ray scaling method, which is described in detail in Gliozzi et al. (2011). The method's basic assumption is that the physics of BH systems is scale-invariant, which means we can calculate the BH mass of an AGN by comparing it to a known stellar-mass GBH that we use as a reference source. More specifically, the method assumes that BH systems undergo the same X-ray spectral evolution
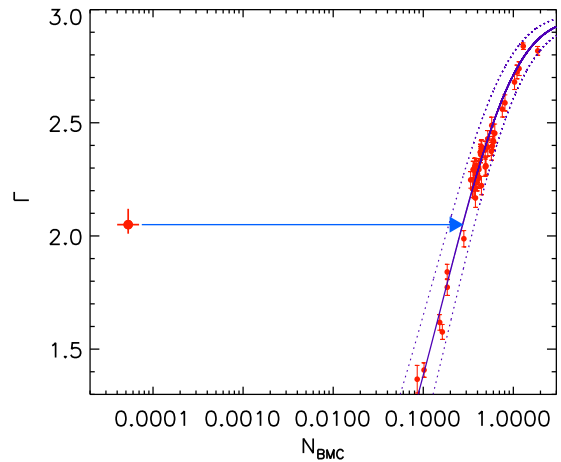

Figure 2. $N_{\rm BMC}$−Γ diagram illustrating the scaling method for an AGN (in this case, Ton S180), represented by the large filled-in circle on the left-hand side, with the reference source XTE J1550−564, whose spectral trend is fitted by the solid curve on the right-hand side. The dotted lines indicate the 1σ uncertainties on the best-fitting function.

associated with changes in accretion rates. For stellar-mass BHs the evolution from low-hard state to high-soft state and vice versa is well documented and can be illustrated by the similar trends shown by different sources when Γ is plotted versus $N_{\rm BMC}$ (Shaposhnikov & Titarchuk 2009). For AGNs, the time-scales for spectral evolution are much longer; therefore, there is only one data point in the $N_{\rm BMC}$−Γ plot, and it can be directly compared to the trend shown by stellar-mass BHs. This procedure is illustrated in Fig. 2, where the large filled-in circle on the left-hand side represents the location of the AGN (in this example, the NLS1 Ton S180) in the $N_{\rm BMC}$−Γ plot, and the data points on the right-hand side represent the spectral evolution of the reference source XTE J1550−564 during the 1998 outburst, which are well fitted by a function indicated by the continuous line (the mathematical expression of this best-fitting function along with the fitting functions of other reference sources are reported in Gliozzi et al. 2011). The scaling factor is provided by the ratio $N_{\rm BMC, t}/N_{\rm BMC, r}$, which is illustrated by the horizontal arrow in Fig. 2. The t subscript denotes the target AGN, and the r subscript denotes the reference source. Since $N_{\rm BMC}$ is directly proportional to the accretion luminosity of the BH system, which in turns depends on $M_{\rm BH}$ and $\dot{m}$, and since Γ defines the accretion state of the source, comparing the $N_{\rm BMC}$ values of target and reference, obtained for the same value of Γ, yields the scaling factor for the BH mass. In this method, the statistical errors on $M_{\rm BH}$ depend on the uncertainties of the AGN position (illustrated by the vertical and horizontal error bars in Fig. 2) as well as on the uncertainties of the functional

Table 3. NLS1 BH masses.

Name (1)	XTE J1550−564 log M_{BH} (2)	GRO J1655−40 log M_{BH} (3)	GX 339−4 log M_{BH} (4)	RM log M_{BH} (5)
Mrk 335	7.45	7.49	7.65	7.230 (1, 2, 3)
I Zw 1	7.91	–	–	–
Ton S180	7.62	–	7.75	–
Mrk 359	6.93	7.10	7.30	–
Mrk 1014	7.86	–	8.01	–
Mrk 586	7.94	–	–	–
Mrk 1044	6.92	6.92	7.12	–
RBS 416	7.25	7.20	7.43	–
HE 0450−2958	8.59	–	8.75	–
PKS 0558−504	8.99	–	9.17	–
Mrk 110	8.16	8.32	8.51	7.292 (1, 4)
PG 0953+414	8.75	8.78	8.95	8.333 (1, 5)
RE J1034+396	7.00	–	7.17	–
PG 1115+407	8.00	–	8.18	–
PG 1116+215	8.50	8.58	8.73	–
NGC 4051	5.86	6.11	6.42	6.130 (6)
PG 1211+143	7.67	–	7.83	–
Mrk 766	6.77	–	6.93	6.822 (7)
Was 61	7.64	–	–	–
PG 1244+026	7.38	–	–	–
PG 1322+659	8.28	–	8.31	–
MCG−6−30−15	7.16	7.21	7.37	–
IRAS 13349+2438	7.79	–	–	–
PG 1402+261	8.30	8.40	8.56	–
NGC 5506	7.02	7.12	7.28	–
PG 1440+356	7.57	–	7.75	–
PG 1448+273	7.77	–	–	–
Mrk 493	6.64	6.59	6.83	–
IRAS 17020+4544	7.79	–	–	–
PDS 456	8.40	–	8.53	–
Mrk 896	6.73	–	6.90	–
Mrk 1513	7.56	7.70	7.87	7.433 (1, 2)
II Zw 177	7.06	–	–	–
Ark 564	7.37	–	–	–
AM 2354−304	6.79	–	–	–

Note: Columns: 1 = AGN name. 2 = Log of BH mass scaled with reference source XTE J1550−564. 3 = Same for reference source GRO J1655−40. 4 = Same for reference source GX 339−4. 5 = Log of BH mass obtained with RM (source: Georgia State University's AGN Black Hole Mass Database; Bentz & Katz (2015). References for RM values: (1) Peterson et al. (2004), (2) Grier et al. (2012), (3) Du et al. (2014), (4) Kollatschny et al. (2001), (5) Kaspi et al. (2000), (6) Denney et al. (2009), (7) Bentz et al. (2010).

representation (illustrated by the dotted lines in the figure). For the values of log(M_{BH}) of the AGNs in this work, derived using XTE J1550−564 as reference source (reported in Tables 3 and 4), the average error is 0.3 dex.

The BH mass of each AGN is determined with the following equation:

$$M_{BH,t} = M_{BH,r} \times \frac{N_{BMC,t}}{N_{BMC,r}} \times \left(\frac{d_t}{d_r}\right)^2, \qquad (1)$$

where d_t/d_r is the ratio of the distances to the target AGN and the reference source.

Tables 3 and 4 list the BH masses obtained with this X-ray scaling method. The RM column in the tables is the M_{BH} obtained by RM and is included for comparison.

When applying the X-ray scaling method to AGNs, we cannot know a priori which of the reference spectral trends better represent the spectral evolution of a specific AGN, since the latter yields only one isolated point in the N_{BMC}–Γ plot. However, only the spectral trend of the reference XTE J1550−564 can be compared to NLS1s

that are characterized by steep Γ values. Therefore, we regard XTE J1550−564 as our primary reference source in this work, since it allows the determination of M_{BH} for all the objects in our samples. For completeness, we also use two other reference sources, GRO J1655−40 and GX 339−4, and report the M_{BH} values obtained with those reference sources as well. The similarity of the M_{BH} values obtained with different reference sources demonstrates that our conclusions do not depend on the specific choice of reference source. Note that based on the analysis from Gliozzi et al. (2011), all reference sources are consistent with each other, but XTE J1550−564 has a tendency to provide M_{BH} systematically lower by a factor of 3, compared to the values obtained with GRO J1655−40 and GX 339−4. Therefore, the M_{BH} values reported in Tables 3 and 4 obtained using the reference source XTE J1550−564 have been increased by a factor of 3.

This method was systematically applied to all AGNs in our samples. The only exceptions are the AGNs that have Γ with unphysically low values, which cannot be compared with any of our reference sources. These are AGNs whose X-ray emission is dominated

Table 4. BLS1 BH masses.

Name (1)	XTE J1550−564 log M_{BH} (2)	GRO J1655−40 log M_{BH} (3)	GX 339−4 log M_{BH} (4)	RM log M_{BH} (5)
PG 0052+251	8.65	8.73	8.88	8.462 (1, 2)
Q 0056−363	9.48	9.58	9.73	–
Mrk 1152	7.76	8.10	8.68	–
ESO 244−G17	6.78	6.92	7.10	–
Fairall 9	8.18	8.27	8.42	8.299 (1, 3, 4)
Mrk 590	7.24	7.45	7.71	7.570 (1)
ESO 198−G24	7.93	8.12	8.36	–
Fairall 1116	7.74	7.82	7.97	–
1H 0419−577	8.82	9.01	9.25	–
3C 120	8.27	8.42	8.60	7.745 (1, 5, 6)
H 0439−272	8.20	8.33	8.50	–
MCG−01−13−25	7.13	7.37	7.66	–
Ark 120	8.18	8.27	8.43	8.068 (1, 7)
MCG−02−14−09	7.07	7.18	7.34	–
MCG+8−11−11	7.90	8.15	8.46	–
H 0557−385	8.13	8.25	8.42	–
PMN J0623−6436	8.46	8.63	8.84	–
ESO 209−G12	7.65	7.77	7.93	–
PG 0804+761	8.36	–	8.52	8.735 (1, 2)
Fairall 1146	7.61	7.70	7.85	–
PG 0844+349	7.29	7.29	7.48	7.858 (1, 2)
MCG+04−22−42	7.83	7.97	8.15	–
PG 0947+396	8.56	8.72	8.92	–
HE 1029−1401	8.59	8.66	8.82	–
PG 1048+342	8.17	8.30	8.47	–
NGC 3516	7.46	7.51	7.67	7.395 (8)
PG 1114+445	8.49	8.63	8.79	–
NGC 3783	7.45	7.68	7.95	7.371 (9, 10, 11)
HE 1143−1810	8.14	8.29	8.48	–
PG 1202+281	8.72	8.92	9.15	–
Mrk 205	8.10	–	8.27	–
Ark 374	7.80	7.90	8.05	–
NGC 4593	7.35	7.57	7.83	6.882 (12, 13)
PG 1307+085	8.27	8.47	8.70	8.537 (1, 2)
4U 1344−60	6.64	6.94	7.35	–
IC 4329A	8.03	8.19	8.39	–
Mrk 279	7.96	8.12	8.30	7.435 (1, 14, 15)
PG 1352+183	9.25	–	–	–
PG 1415+451	7.74	7.79	7.95	–
NGC 5548	7.83	8.32	–	7.718 (1, 8, 16, 17, 18, 19, 20, 21)
PG 1416−129	8.68	8.98	9.39	–
PG 1425+267	9.10	9.31	9.57	–
Mrk 1383	9.05	8.84	8.62	9.007 (1, 2)
PG 1427+480	8.63	8.63	8.82	–
Mrk 841	8.58	8.37	8.16	–
Mrk 290	7.40	7.63	7.90	7.277 (8)
Mrk 876	9.51	9.83	10.31	8.339 (1, 2)
PG 1626+554	8.57	8.89	9.37	–
IGR J17418−1212	7.80	7.90	8.06	–
Mrk 509	8.40	8.58	8.80	8.049 (1)
Mrk 304	7.50	7.59	7.74	–
MR 2251−178	8.88	9.15	9.49	–
NGC 7469	7.20	7.38	7.59	6.956 (22, 23, 24)
Mrk 926	8.41	8.60	8.82	–

Note: Columns: 1 = AGN name. 2 = Log of BH mass scaled with reference source XTE J1550−564. 3 = Same for reference source GRO J1655−40. 4 = Same for reference source GX 339−4. 5 = Log of BH mass obtained with RM (source: Georgia State University's AGN Black Hole Mass Database; Bentz & Katz (2015). References for RM values: (1) Peterson et al. (2004), (2) Kaspi et al. (2000), (3) Santos-Lleo et al. (1997), (4) Rodriguez-Pascual et al. (1997), (5) Kollatschny et al. (2014), (6) Grier et al. (2012), (7) Doroshenko, Sergeev & Pronik (2008), (8) Denney et al. (2010), (9) Stirpe et al. (1994), (10) Onken & Peterson (2002), (11) Reichert et al. (1994), (12) Denney et al. (2006), (13) Barth et al. (2010), (14) Maoz et al. (1990), (15) Santos-Lleo et al. (2001), (16) Netzer et al. (1990), (17) Kovacevik et al. (2014), (18) Bentz et al. (2010), (19) Dietrich et al. (1993), (20) Clavel et al. (1991), (21) Korista et al. (1995), (22) Collier et al. (1998), (23) Peterson et al. (2014), (24) Wanders et al. (1997).

Table 5. NLS1 BH accretion rates.

Name (1)	XTE J1550−564 L_X/L_{Edd} (2)	L_{bol}/L_{Edd} (3)	GRO J1655−40 L_X/L_{Edd} (4)	L_{bol}/L_{Edd} (5)	GX 339−4 L_X/L_{Edd} (6)	L_{bol}/L_{Edd} (7)
Mrk 335	2.59×10^{-3}	5.10×10^{-1}	2.39×10^{-3}	4.70×10^{-1}	1.62×10^{-3}	3.20×10^{-1}
I Zw 1	6.45×10^{-3}	6.21×10^{-1}	–	–	–	–
Ton S180	6.51×10^{-3}	6.28×10^{-1}	–	–	4.73×10^{-3}	4.56×10^{-1}
Mrk 359	4.22×10^{-3}	4.07×10^{-1}	2.87×10^{-3}	2.77×10^{-1}	1.81×10^{-3}	1.74×10^{-1}
Mrk 1014	6.82×10^{-3}	6.58×10^{-1}	–	–	4.76×10^{-3}	4.59×10^{-1}
Mrk 586	8.88×10^{-3}	8.56×10^{-1}	–	–	–	–
Mrk 1044	5.86×10^{-3}	5.65×10^{-1}	5.86×10^{-3}	5.65×10^{-1}	3.76×10^{-3}	3.62×10^{-1}
RBS 416	6.95×10^{-3}	6.70×10^{-1}	7.85×10^{-3}	7.57×10^{-1}	4.53×10^{-3}	4.37×10^{-1}
HE 0450−2958	7.35×10^{-3}	7.09×10^{-1}	–	–	5.07×10^{-3}	4.89×10^{-1}
PKS 0558−504	5.95×10^{-3}	5.74×10^{-1}	–	–	3.91×10^{-3}	3.77×10^{-1}
Mrk 110	4.38×10^{-3}	8.07×10^{-2}	3.03×10^{-3}	5.57×10^{-2}	1.93×10^{-3}	3.56×10^{-2}
PG 0953+414	6.40×10^{-3}	6.17×10^{-1}	6.03×10^{-3}	5.81×10^{-1}	4.04×10^{-3}	3.90×10^{-1}
RE J1034+396	2.73×10^{-3}	2.64×10^{-1}	–	–	1.85×10^{-3}	1.78×10^{-1}
PG 1115+407	1.97×10^{-2}	1.90	–	–	1.30×10^{-2}	1.25
PG 1116+215	6.30×10^{-3}	6.07×10^{-1}	5.22×10^{-3}	5.04×10^{-1}	3.69×10^{-3}	3.56×10^{-1}
NGC 4051	1.48×10^{-3}	6.08×10^{-2}	8.28×10^{-4}	3.40×10^{-2}	4.05×10^{-4}	1.67×10^{-2}
PG 1211+143	8.55×10^{-3}	1.85	–	–	5.96×10^{-3}	1.29
Mrk 766	7.43×10^{-3}	7.17×10^{-1}	–	–	5.18×10^{-3}	5.00×10^{-1}
Was 61	4.62×10^{-3}	4.46×10^{-1}	–	–	–	–
PG 1244+026	4.49×10^{-3}	4.33×10^{-1}	–	–	–	–
PG 1322+659	4.79×10^{-3}	4.62×10^{-1}	–	–	4.54×10^{-3}	4.37×10^{-1}
MCG−6−30−15	2.19×10^{-3}	2.11×10^{-1}	1.95×10^{-3}	1.88×10^{-1}	1.35×10^{-3}	1.30×10^{-1}
IRAS 13349+2438	1.20×10^{-2}	1.16	–	–	–	–
PG 1402+261	4.28×10^{-3}	4.13×10^{-1}	3.34×10^{-3}	3.22×10^{-1}	2.33×10^{-3}	2.24×10^{-1}
NGC 5506	8.10×10^{-3}	7.81×10^{-1}	6.37×10^{-3}	6.14×10^{-1}	4.46×10^{-3}	4.30×10^{-1}
PG 1440+356	5.57×10^{-3}	5.37×10^{-1}	–	–	3.67×10^{-3}	3.53×10^{-1}
PG 1448+273	3.62×10^{-3}	3.49×10^{-1}	–	–	–	–
Mrk 493	6.87×10^{-3}	6.62×10^{-1}	7.77×10^{-3}	7.49×10^{-1}	4.48×10^{-3}	4.32×10^{-1}
IRAS 17020+4544	6.71×10^{-3}	6.47×10^{-1}	–	–	–	–
PDS 456	7.91×10^{-3}	7.62×10^{-1}	–	–	5.85×10^{-3}	5.64×10^{-1}
Mrk 896	8.31×10^{-3}	8.01×10^{-1}	–	–	5.67×10^{-3}	5.46×10^{-1}
Mrk 1513	6.91×10^{-3}	6.67×10^{-1}	5.08×10^{-3}	4.90×10^{-1}	3.42×10^{-3}	3.29×10^{-1}
II Zw 177	1.07×10^{-2}	1.03	–	–	–	–
Ark 564	9.90×10^{-3}	9.55×10^{-1}	–	–	–	–
AM 2354−304	8.52×10^{-3}	8.21×10^{-1}	–	–	–	–

Note: Columns: 1 = AGN name. 2 = Ratio of X-ray luminosity (2–10 keV) to Eddington luminosity scaled with XTE J1550−564. 3 = Ratio of bolometric luminosity to Eddington luminosity scaled with XTE J1550−564. 4–5 = Same for reference source GRO J1655−40. 6–7 = Same for reference source GX 339−4.

by reflection or absorption or both and hence cannot be compared with the primary coronal emission of the reference sources. As we mentioned in Section 3, nine of the AGNs were in this category, leaving us with a total of 89 AGNs.

Next we move to a comparison of NLS1s and BLS1s by accretion rate rather than M_{BH}, and our results are shown in Tables 5 and 6. We used two proxies for accretion rate. The first is the ratio of the X-ray luminosity L_X derived in our spectral analysis to the Eddington luminosity L_{Edd} obtained from the M_{BH} values. The second is the ratio of bolometric luminosity L_{bol} to L_{Edd}. To determine the bolometric luminosity of all our objects, we used the correction factors derived by Vasudevan & Fabian (2009) by fitting broad-band spectral energy distributions (SEDs) obtained with simultaneous data from a sizable sample of AGNs. More specifically, for objects in our samples that are also in the Vasudevan and Fabian sample, we used the specific bolometric correction values derived from their SED fitting. For all the other objects, we used average correction factors that we obtained by averaging separately the NLS1s and BLS1s in the Vasudevan and Fabian sample. For NLS1s, the average bolometric correction is 96.4, whereas for BLS1s it is 23.7.

Tables 3–6, then, list the three numbers, M_{BH}, L_X/L_{Edd}, and L_{bol}/L_{Edd}, for each AGN using all three reference sources. An ellipsis in the tables denotes that the value of Γ for that AGN, as derived by the XSPEC fit, fell outside the known range of Γ for the reference source and, therefore, that source could not be used in the scaling process to determine M_{BH} for that particular AGN.

The results of our analysis are illustrated in Figs 3–5. Fig. 3 shows the distribution of NLS1s and BLS1s by BH mass. The number of NLS1s is shown by a solid line (blue in the online version), and the number of BLS1s, by a dashed line (red online). Fig. 4 shows the distribution of NLS1s and BLS1s by the ratio L_X/L_{Edd}. Finally, Fig. 5 compares NLS1s and BLS1s by L_{bol}/L_{Edd}. A visual inspection of Figs 3–5 suggests that the distributions of M_{BH}, L_X/L_{Edd}, and L_{bol}/L_{Edd} of NLS1s are different from the respective distributions of BLS1s. This conclusion was confirmed by statistical tests, whose results are summarized in Table 7. The top half of the table shows the differences between NLS1s and BLS1s in their average values for each parameter. Each number in the bottom half of the table is the probability of finding a difference this large given the null hypothesis that our samples of NLS1s and BLS1s were taken from the

Table 6. BLS1 BH accretion rates.

Name (1)	XTE J1550−564 L_X/L_{Edd} (2)	L_{bol}/L_{Edd} (3)	GRO J1655−40 L_X/L_{Edd} (4)	L_{bol}/L_{Edd} (5)	GX 339−4 L_X/L_{Edd} (6)	L_{bol}/L_{Edd} (7)
PG 0052+251	5.82×10^{-3}	1.14×10^{-1}	4.87×10^{-3}	9.50×10^{-2}	3.44×10^{-3}	6.72×10^{-2}
Q 0056−363	4.80×10^{-4}	1.14×10^{-2}	3.84×10^{-4}	9.09×10^{-3}	2.70×10^{-4}	6.40×10^{-3}
Mrk 1152	4.04×10^{-3}	9.60×10^{-2}	1.84×10^{-3}	4.36×10^{-2}	4.79×10^{-4}	1.14×10^{-2}
ESO 244−G17	4.59×10^{-3}	1.09×10^{-1}	3.33×10^{-3}	7.92×10^{-2}	2.22×10^{-3}	5.28×10^{-2}
Fairall 9	5.54×10^{-3}	5.82×10^{-2}	4.55×10^{-3}	4.78×10^{-2}	3.22×10^{-3}	3.38×10^{-2}
Mrk 590	4.46×10^{-3}	3.12×10^{-2}	2.71×10^{-3}	1.90×10^{-2}	1.50×10^{-3}	1.05×10^{-2}
ESO 198−G24	4.45×10^{-3}	1.06×10^{-1}	2.83×10^{-3}	6.71×10^{-2}	1.65×10^{-3}	3.92×10^{-2}
Fairall 1116	5.93×10^{-3}	1.41×10^{-1}	4.87×10^{-3}	1.16×10^{-2}	3.44×10^{-3}	8.17×10^{-2}
1H 0419−577	3.99×10^{-3}	9.48×10^{-2}	2.54×10^{-3}	6.02×10^{-2}	1.48×10^{-3}	3.52×10^{-2}
3C 120	4.52×10^{-3}	9.30×10^{-2}	3.24×10^{-3}	6.68×10^{-2}	2.14×10^{-3}	4.41×10^{-2}
H 0439−272	4.67×10^{-3}	1.11×10^{-1}	3.47×10^{-3}	8.25×10^{-2}	2.35×10^{-3}	5.59×10^{-2}
MCG−01−13−25	3.96×10^{-3}	9.41×10^{-2}	2.29×10^{-3}	5.43×10^{-2}	1.17×10^{-3}	2.79×10^{-2}
Ark 120	4.52×10^{-3}	1.07×10^{-1}	3.61×10^{-3}	8.58×10^{-2}	2.54×10^{-3}	6.04×10^{-2}
MCG−02−14−09	5.07×10^{-3}	1.20×10^{-1}	3.88×10^{-3}	9.20×10^{-2}	2.68×10^{-3}	6.36×10^{-2}
MCG+8−11−11	4.09×10^{-3}	9.71×10^{-2}	2.29×10^{-3}	5.44×10^{-2}	1.12×10^{-3}	2.66×10^{-2}
H 0557−385	6.30×10^{-3}	1.50×10^{-1}	4.72×10^{-3}	1.12×10^{-1}	3.22×10^{-3}	7.65×10^{-2}
PMN J0623−6436	4.03×10^{-3}	9.58×10^{-2}	2.71×10^{-3}	6.41×10^{-2}	1.68×10^{-3}	3.97×10^{-2}
ESO 209−G12	5.36×10^{-3}	1.27×10^{-1}	4.10×10^{-3}	9.74×10^{-2}	2.83×10^{-3}	6.73×10^{-2}
PG 0804+761	6.17×10^{-4}	1.47×10^{-2}	–	–	4.26×10^{-4}	1.01×10^{-2}
Fairall 1146	5.62×10^{-3}	1.34×10^{-1}	4.58×10^{-3}	1.09×10^{-1}	3.23×10^{-3}	7.68×10^{-2}
PG 0844+349	7.24×10^{-3}	5.21×10^{-1}	7.24×10^{-3}	5.21×10^{-1}	4.65×10^{-3}	1.10×10^{-1}
MCG+04−22−42	4.35×10^{-3}	1.03×10^{-1}	3.13×10^{-3}	7.42×10^{-2}	2.06×10^{-3}	4.90×10^{-2}
PG 0947+396	4.35×10^{-3}	1.03×10^{-1}	3.01×10^{-3}	7.13×10^{-2}	1.92×10^{-3}	1.38×10^{-1}
HE 1029−1401	6.36×10^{-3}	1.51×10^{-1}	5.33×10^{-3}	1.26×10^{-1}	3.76×10^{-3}	8.94×10^{-2}
PG 1048+342	5.17×10^{-3}	1.23×10^{-1}	3.84×10^{-3}	9.10×10^{-2}	2.60×10^{-3}	6.16×10^{-2}
NGC 3516	2.07×10^{-3}	3.16×10^{-2}	1.81×10^{-3}	2.77×10^{-2}	1.27×10^{-3}	2.00×10^{-2}
PG 1114+445	2.96×10^{-3}	7.02×10^{-2}	2.17×10^{-3}	5.15×10^{-2}	1.50×10^{-3}	3.57×10^{-2}
NGC 3783	3.27×10^{-3}	5.17×10^{-2}	1.94×10^{-3}	3.07×10^{-2}	1.04×10^{-3}	8.00×10^{-3}
HE 1143−1810	3.94×10^{-3}	9.35×10^{-2}	2.76×10^{-3}	6.56×10^{-2}	1.78×10^{-3}	4.24×10^{-2}
PG 1202+281	3.78×10^{-3}	8.96×10^{-2}	2.40×10^{-3}	5.68×10^{-2}	1.40×10^{-3}	3.32×10^{-2}
Mrk 205	8.49×10^{-3}	2.02×10^{-1}	–	–	5.79×10^{-3}	1.38×10^{-1}
Ark 374	4.00×10^{-3}	9.50×10^{-2}	3.23×10^{-3}	7.67×10^{-2}	2.28×10^{-3}	5.41×10^{-2}
NGC 4593	1.50×10^{-3}	1.15×10^{-2}	9.11×10^{-4}	7.01×10^{-3}	5.04×10^{-3}	2.12×10^{-2}
PG 1307+085	4.55×10^{-3}	1.59×10^{-1}	2.89×10^{-3}	1.01×10^{-1}	1.69×10^{-3}	4.00×10^{-2}
4U 1344−60	3.76×10^{-3}	8.94×10^{-2}	1.89×10^{-3}	4.48×10^{-2}	7.26×10^{-4}	1.72×10^{-2}
IC 4329A	4.13×10^{-3}	9.80×10^{-2}	2.81×10^{-3}	6.68×10^{-2}	1.77×10^{-3}	4.20×10^{-2}
Mrk 279	4.27×10^{-3}	8.67×10^{-2}	2.95×10^{-3}	6.00×10^{-2}	1.95×10^{-3}	3.97×10^{-2}
PG 1352+183	1.30×10^{-3}	3.08×10^{-2}	–	–	–	–
PG 1415+451	5.07×10^{-3}	1.21×10^{-1}	4.45×10^{-3}	1.05×10^{-1}	3.11×10^{-3}	1.09×10^{-1}
NGC 5548	2.14×10^{-3}	2.16×10^{-2}	6.98×10^{-4}	5.37×10^{-3}	–	–
PG 1416−129	3.06×10^{-4}	7.27×10^{-3}	1.53×10^{-4}	3.64×10^{-3}	5.90×10^{-5}	1.40×10^{-3}
PG 1425+267	3.69×10^{-3}	8.77×10^{-2}	2.25×10^{-3}	5.32×10^{-2}	1.24×10^{-3}	2.94×10^{-2}
Mrk 1383	1.06×10^{-3}	2.51×10^{-2}	1.69×10^{-3}	4.02×10^{-2}	2.80×10^{-3}	6.63×10^{-2}
PG 1427+480	3.80×10^{-3}	9.02×10^{-2}	3.80×10^{-3}	9.01×10^{-2}	2.44×10^{-3}	5.78×10^{-2}
Mrk 841	9.38×10^{-4}	2.23×10^{-2}	1.50×10^{-3}	3.55×10^{-2}	2.48×10^{-3}	5.87×10^{-2}
Mrk 290	4.57×10^{-3}	1.09×10^{-1}	2.71×10^{-3}	6.42×10^{-2}	1.45×10^{-3}	3.43×10^{-2}
Mrk 876	8.70×10^{-4}	2.07×10^{-2}	4.16×10^{-4}	9.87×10^{-3}	1.38×10^{-4}	3.27×10^{-3}
PG 1626+554	2.91×10^{-3}	6.92×10^{-2}	1.39×10^{-3}	3.31×10^{-2}	4.63×10^{-4}	1.10×10^{-2}
IGR J17418−1212	5.10×10^{-3}	1.21×10^{-1}	4.04×10^{-3}	9.60×10^{-2}	2.84×10^{-3}	6.74×10^{-2}
Mrk 509	4.29×10^{-3}	6.95×10^{-2}	2.83×10^{-3}	4.58×10^{-2}	1.72×10^{-3}	2.79×10^{-2}
Mrk 304	1.03×10^{-2}	2.44×10^{-1}	8.29×10^{-3}	1.96×10^{-1}	5.85×10^{-3}	1.39×10^{-1}
MR 2251−178	4.31×10^{-3}	1.02×10^{-1}	2.34×10^{-3}	5.55×10^{-2}	1.08×10^{-3}	2.55×10^{-2}
NGC 7469	8.66×10^{-3}	3.64×10^{-1}	5.81×10^{-3}	4.48×10^{-2}	3.60×10^{-3}	5.51×10^{-2}
Mrk 926	4.52×10^{-3}	1.07×10^{-1}	2.93×10^{-3}	6.94×10^{-2}	1.75×10^{-3}	4.14×10^{-2}

Note: Columns: 1 = AGN name. 2 = Ratio of X-ray luminosity (2–10 keV) to Eddington luminosity scaled with XTE J1550−564. 3 = Ratio of bolometric luminosity to Eddington luminosity scaled with XTE J1550−564. 4–5 = Same for reference source GRO J1655−40. 6–7 = Same for reference source GX 339−4.
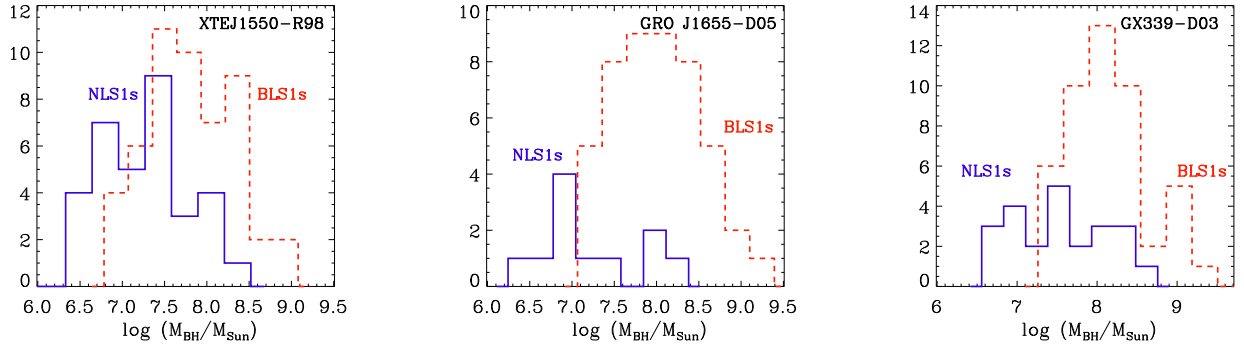
Figure 3. Number of NLS1s and BLS1s by BH mass using reference source XTE J1550−564 (left), GRO J1655−40 (centre), and GX 339−4 (right).
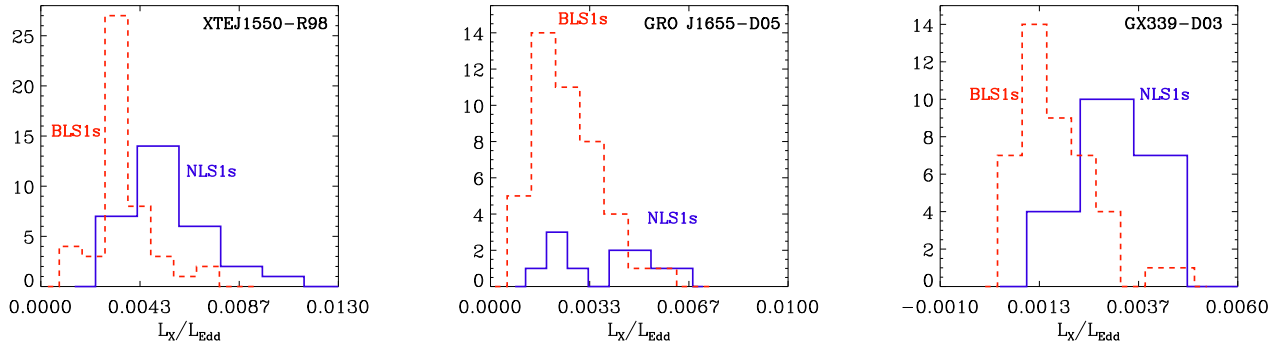

Figure 4. Number of NLS1s and BLS1s by L_X/L_{Edd} using reference source XTE J1550−564 (left), GRO J1655−40 (centre), and GX 339−4 (right).
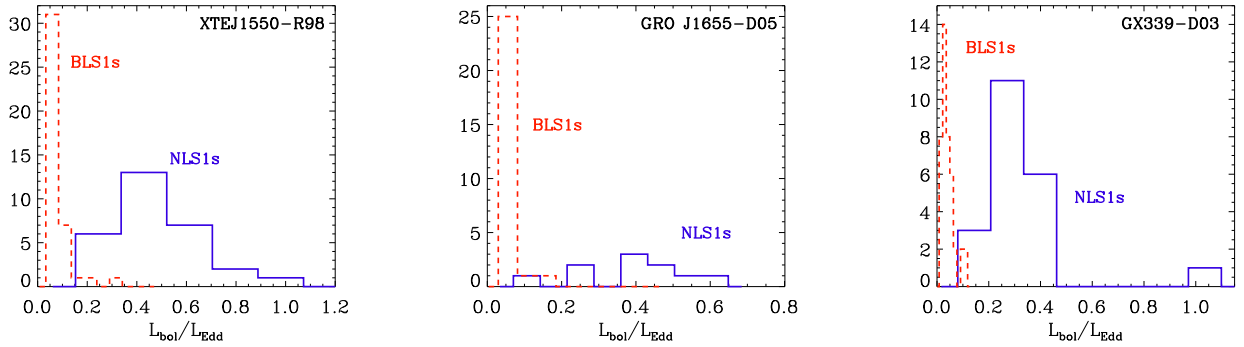

Figure 5. Number of NLS1s and BLS1s by L_{bol}/L_{Edd} using reference source XTE J1550−564 (left), GRO J1655−40 (centre), and GX 339−4 (right).

same population. On average the M_{BH} values of NLS1s are smaller than the corresponding values of BLS1s. The difference between the M_{BH} averages is marginally significant at the 2.6σ level, and a *t*-test indicates that the average M_{BH} values of NLS1s and BLS1s are consistent with being drawn from the same population with a probability of 5 per cent. A difference at higher significance level between the two AGN populations is obtained using a nonparametric Kolmogorov–Smirnov (K–S) test, which indicates that the probability that the distributions of M_{BH} from NLS1s and BLS1s are drawn from the same population is 1 per cent. Differences between NLS1s and BLS1s at even higher significance levels are inferred when the accretion rates are compared: the distributions of both

accretion rate indicators – L_X/L_{Edd} and L_{bol}/L_{Edd} – have less than a 0.01 per cent probability of being drawn from the same population.

5 DISCUSSION AND CONCLUSIONS

In this work, we have carried out a homogeneous spectral analysis of the X-ray data with an absorbed Comptonization model (BMC) of two samples of NLS1s and BLS1s, derived from a flux-limited sample of type I AGNs observed with the *XMM–Newton* satellite. Starting from the spectral-fitting results, we applied an X-ray scaling method to infer the BH masses and accretion rate values.

Our statistical analysis, based on a K–S test, reveals that the BH

Table 7. Statistical comparison of NLS1s and BLS1s.

	XTE J1550−564			GRO J1655−40			GX 339−4		
	M_{BH} ($\times 10^8$ M$_\odot$)	L_X/L_{Edd} ($\times 10^{-3}$)	L_{bol}/L_{Edd} ($\times 10^{-1}$)	M_{BH} ($\times 10^8$ M$_\odot$)	L_X/L_{Edd} ($\times 10^{-3}$)	L_{bol}/L_{Edd} ($\times 10^{-1}$)	M_{BH} ($\times 10^8$ M$_\odot$)	L_X/L_{Edd} ($\times 10^{-3}$)	L_{bol}/L_{Edd} ($\times 10^{-1}$)
NLS1s	1.1	6.7	6.7	1.2	4.5	4.3	2.2	4.1	4.2
BLS1s	3.5	4.2	1.0	5.0	3.1	0.7	10	2.1	0.5
Prob (K–S)	1.0×10^{-2}	$<10^{-4}$	$<10^{-4}$	1.1×10^{-2}	1.6×10^{-2}	$<10^{-4}$	8.0×10^{-3}	$<10^{-4}$	$<10^{-4}$
Prob (t)	3.6×10^{-2}	$<10^{-4}$	$<10^{-4}$	2.2×10^{-1}	1.0×10^{-2}	1.0×10^{-4}	1.8×10^{-1}	$<10^{-4}$	$<10^{-4}$

Note: Row 1 shows the mean values of M_{BH}, L_X/L_{Edd}, and L_{bol}/L_{Edd} for NLS1s. Row 2 shows the mean values for BLS1s. Row 3 uses a K–S test to give the probability of finding differences this large given the null hypothesis that NLS1s and BLS1s come from the same population. Row 4 gives the same probability, but this time using a Student's t-test. Using reference source XTE J1550−564, we were able to compare 35 NLS1s and 54 BLS1s. Using reference source GRO J1655−40, we compared 13 NLS1s and 51 BLS1s. Using reference source GX 339−4, we compared 25 NLS1s and 51 BLS1s.
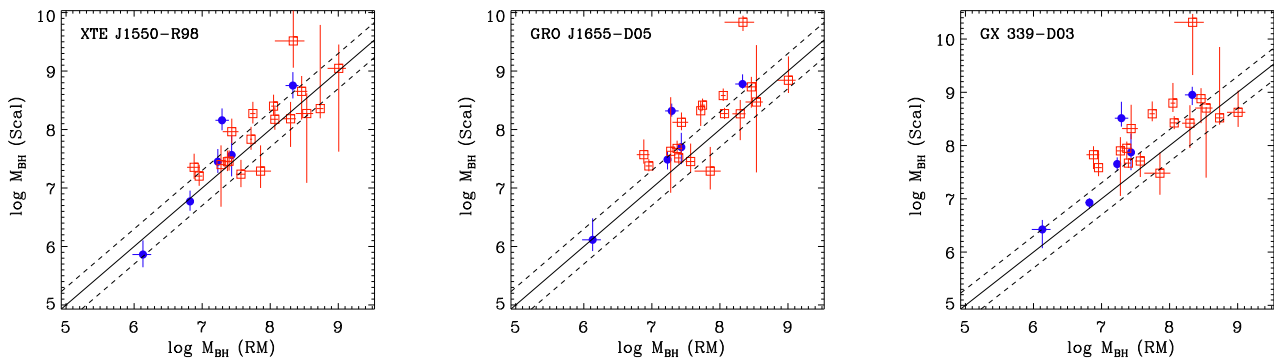
Figure 6. Comparison of RM with the X-ray scaling method using reference source XTE J1550−564 (left), GRO J1655−40 (centre), and GX 339−4 (right). NLS1s are shown with filled-in circles (blue in the online version), and BLS1s are shown with open squares (red online). The y-axis shows log M_{BH} derived from the X-ray scaling method. The x-axis shows log M_{BH} derived from RM. The dashed lines represent the 0.3 dex levels, commonly assumed as uncertainty on the RM estimates.

mass distributions of NLS1s and BLS1s, despite a substantial overlap (see Fig. 3 and Table 7), are inconsistent with the hypothesis that the two classes are drawn from the same population at the 99 per cent significance level. Similar results (i.e. a clear distinction between NLS1s and BLS1s) with an even higher statistical significance are obtained when the accretion rate indicators (parametrized by L_X/L_{Edd} and by L_{bol}/L_{Edd}) of the NLS1 and BLS1 populations are compared (see Figs 4 and 5, and Table 7).

One of the motivations of our work was to constrain M_{BH} of NLS1s and BLS1s with a method that, unlike the optically based techniques, does not make any assumptions about the BLR geometry and dynamics. It is therefore interesting to compare our results with the M_{BH} values constrained with the RM method. To this end, we used Georgia State University's AGN Black Hole Mass Database (Bentz & Katz 2015), which contains all M_{BH} values reported in peer-reviewed articles and has 24 objects in common with our samples.

This comparison is illustrated in Fig. 6, where the log of the M_{BH} values derived using the X-ray scaling method are plotted versus the corresponding values determined from RM. The filled-in circles (blue in the online version) represent NLS1s, whereas the open squares (red online) represent BLS1s. A visual inspection of these plots suggests a broad agreement between the M_{BH} values obtained with the two methods for both NLS1s and BLS1s. From a closer look at these plots, it appears that NLS1 M_{BH} values obtained with the X-ray scaling method tend to lie above the one-to-one correlation

line, whereas the BLS1 values seem to be more uniformly distributed around the one-to-one correlation. To compare the M_{BH} values obtained with these two methods in a more quantitative way, we computed the average ratios between the values determined with the scaling method and the reverberation method for NLS1s and BLS1s separately. Using the three different reference sources, we obtained: $\langle M_{BH, scal}/M_{BH, RM} \rangle = 1.03 \pm 0.02$ and 1.02 ± 0.01 for NLS1s and BLS1s, respectively, using XTE J1550−564 as reference, 1.05 ± 0.02 and 1.04 ± 0.01 using GRO J1655−40, and 1.07 ± 0.02 and 1.06 ± 0.02 using GX 339−4. The ratios of NLS1 values are statistically indistinguishable from the BLS1 values. This result, besides confirming the agreement between the X-ray scaling and RM, may suggest that the BLR dynamics is not strongly affected by radiation pressure and RM can be safely applied also to NLS1s in general. However, we must note that none of the NLS1s that are common to our sample and the RM one are accreting at or above the Eddington limit. We can therefore only conclude that the effect of the radiation pressure on the BLR dynamics is moderate and that RM can be safely used for this limited sample of moderately accreting NLS1s.

We also investigated whether our NLS1 sample can be considered homogeneous. To this end, we separated the NLS1s that have detected radio structures from those that have no radio detection (note that none of the objects with extended radio structure is classified as very radio-loud or has gamma-ray detections). We then compared these two subsamples of NLS1s: although the NLS1s with radio

detections have slightly larger $M_{\rm BH}$ values, their average values are consistent within 1σ and the two distributions are indistinguishable based on a K–S test (with a probability of >90 per cent).

Based on these results we can conclude that indeed NLS1s are characterized by different distributions of $M_{\rm BH}$ and accretion rates than 'normal' BLS1s. This is in agreement with the hypothesis that NLS1s represent a younger phase of AGN activity, when relatively small supermassive BHs grow very rapidly.

However, before drawing any general conclusion one must consider that the sample used in this work is not complete by any means and may not be representative of the entire population of NLS1s. Indeed, the relatively high X-ray luminosity may indicate that the sample is skewed towards bright objects with large $M_{\rm BH}$. Future studies, based on larger and volume-limited samples, will provide more conclusive results on the nature of NLS1s.

ACKNOWLEDGEMENTS

REFERENCES

Arnaud K. A., 1996, in Jacoby G., Barnes J., eds, ASP Conf. Ser. Vol. 101, Astronomical Data Analysis Software and Systems V. Astron. Soc. Pac., San Francisco, p. 17
Barth A. J. et al., 2013, ApJ, 769, 128
Bentz M. C., Katz S., 2015, PASP, 127, 67
Bentz M. C. et al., 2010, ApJ, 716, 993
Boroson T. A., Green R. F., 1992, ApJS, 80, 109B
Clavel J. et al., 1991, ApJ, 366, 64
Collier S. J. et al., 1998, ApJ, 500, 162
Decarli R., Dotti M., Fontana M., Haardt F., 2008, MNRAS, 386, L15
Denney K. D. et al., 2006, ApJ, 653, 152
Denney K. D. et al., 2009, ApJ, 702, 1353
Denney K. D. et al., 2010, ApJ, 721, 715
Dietrich M. et al., 1993, ApJ, 408, 416
Doroshenko V. T., Sergeev S. G., Pronik V. I., 2008, Astron. Rep., 52, 442
Du P. et al., 2014, ApJ, 782, 45

Foschini L. et al., 2015, A&A, 575A, A13
Gliozzi M., Titarchuk L., Satyapal S., Price D., Jang I., 2011, ApJ, 735, 16
Grier C. J. et al., 2012, ApJ, 755, 60
Grupe D., 2004, AJ, 127, 1799
Grupe D., Mathur S., 2004, ApJ, 606, 41
Jang I., Gliozzi M., Satyapal S., Titarchuk L., 2018, MNRAS, 473, 136
Kaspi S., Smith P. S., Netzer H., Maoz D., Jannuzi B. T., Giveon U., 2000, ApJ, 533, 631
Kollatschny W., Bischoff K., Robinson E. L., Welsh W. F., Hill G. J., 2001, A&A, 379, 125
Kollatschny W., Ulbrich K., Zetzl M., Kaspi S., Haas M., 2014, A&A, 566, 106
Korista K. T. et al., 1995, ApJS, 97, 285
Kovacevik A., Popović L. Č., Shapovalova A. I., Ilić D., Burenkov A. N., Chavushyan V. H., 2014, Adv. Space Res., 54, 1414
Maoz D. et al., 1990, ApJ, 351, 75
Marconi A., Axon D. J., Maiolino R., Nagao T., Pastorini G., Pietrini P., Robinson A., Torricelli G., 2008, ApJ, 678, 693
Mathur S., Grupe D., 2005a, A&A, 432, 463
Mathur S., Grupe D., 2005b, ApJ, 633, 688
Netzer H. et al., 1990, ApJ, 353, 108
Onken C. A., Peterson B. M., 2005, ApJ, 572, 746
Peterson B. M., Horne K., 2006, in Livio M., Casertano S., eds, Space Telescope Sci. Inst. Symp. Ser. Vol. 18, Planets to Cosmology: Essential Science in the Final Years of the Hubble Space Telescope . Cambridge Univ. Press, Cambridge, UK
Peterson B. M. et al., 2004, ApJ, 613, 682
Peterson B. M. et al., 2014, ApJ, 795, 149
Reichert G. A. et al., 1994, ApJ, 425, 582
Rodriguez-Pascual P. M. et al., 1997, ApJS, 110, 9
Santos-Lleo M. et al., 1997, ApJS, 112, 271
Santos-Lleo M. et al., 2001, A&A, 369, 57
Shaposhnikov N., Titarchuk L., 2009, ApJ, 699, 453
Stirpe G. M. et al., 1994, ApJ, 425, 609
Strüder L. et al., 2001, A&A, 365, L18
Titarchuk L. G., Mastichiadis A., Kylafis N. D., 1997, ApJ, 487, 834
Turner M. J. L. et al., 2001, A&A, 365, L27
Vasudevan R. V., Fabian A. C., 2009, MNRAS, 392, 1124
Wanders I. et al., 1997, ApJS, 113, 69
Zhou X.-L., Zhang S.-N., 2010, ApJ, 713, L11

This paper has been typeset from a TeX/LaTeX file prepared by the author.